iScience

CellPress
OPEN ACCESS

Article

Efficient fabrication of tilt micro/nanopillars on polypropylene surface with robust superhydrophobicity for directional water droplet rebound

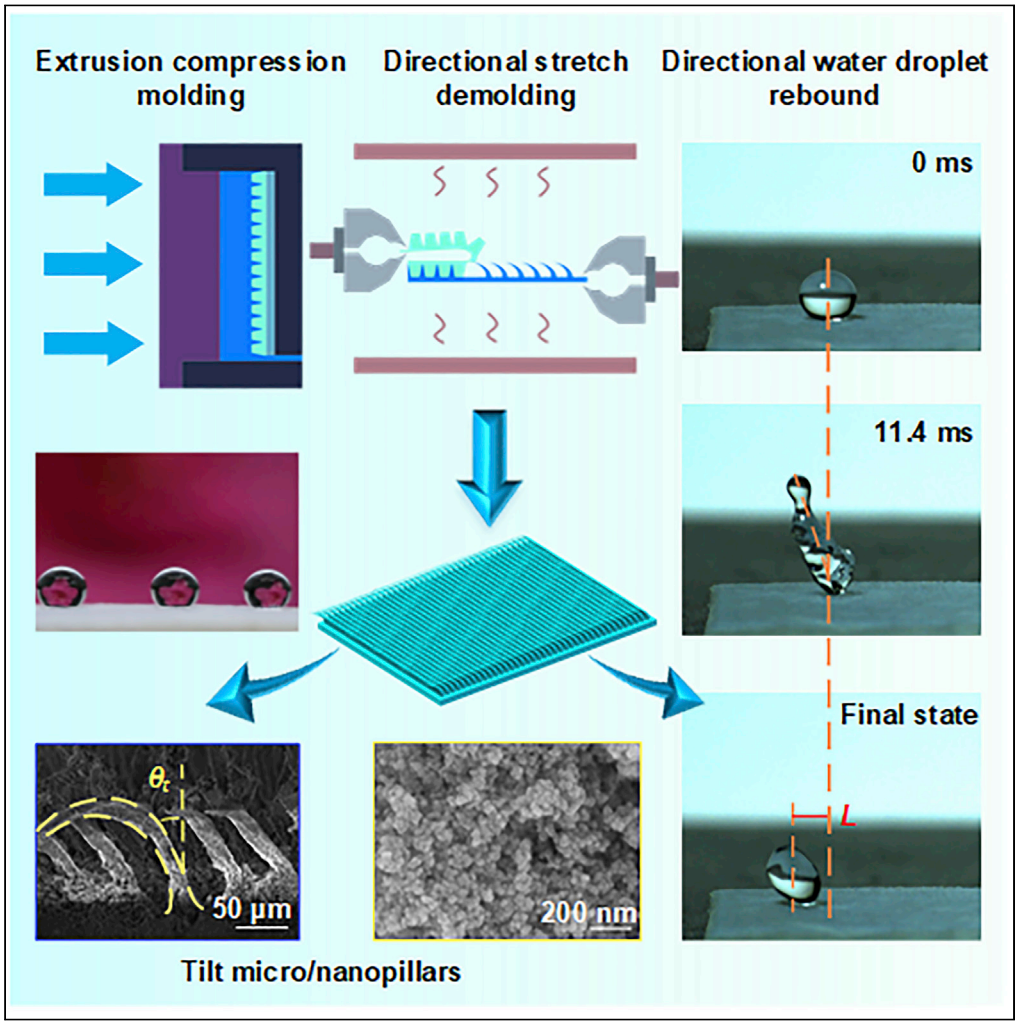

Yu Du, Ting Wu, Xiao-long Li, ..., Xiang Lu, Heng Xie, Jin-ping Qu

hengxie@hust.edu.cn (H.X.)
jpqu@hust.edu.cn (J.-p.Q.)

Highlights

A tilt micro/nanopillars surface is developed and thoroughly characterized

The rolling angle of the surface shows anisotropy in different directions

The directional rebound can be controlled by the energy of the water droplet

The directional rebound can be controlled by the tilt angle of the surface

Du et al., iScience 25, 105107
October 21, 2022
https://doi.org/10.1016/j.isci.2022.105107

iScience

CellPress
OPEN ACCESS

Article

Efficient fabrication of tilt micro/nanopillars on polypropylene surface with robust superhydrophobicity for directional water droplet rebound

Yu Du,[1,2,3] Ting Wu,[1,2,3] Xiao-long Li,[1,2,3] Wei-long Zhou,[1,2,3] Chao Ding,[4] You-qiang Yang,[4] Jin-gang Wei,[4] Xiang Lu,[1,2,3] Heng Xie,[1,2,3,5,*] and Jin-ping Qu[1,2,3,*]

SUMMARY

The directional rebound and transport of water droplets plays an important role in microfluidic devices, anti-fogging, and water harvesting. Herein, an extrusion compression molding and directional stretch demolding method was used to prepare a polypropylene (PP) surface with tilt micro/nanopillars with a contact angle of 157 $\pm$ 3°. The rolling angle is the highest (9 $\pm$ 4°) when the direction of rotation is opposite the tilt direction of the micro/nanopillars, showing excellent water repellency and anisotropy of the surface. Compared with the position of the first collision of the water droplet, the position of the second collision shifted ~1.5 mm along the tilt direction of the micro/nanopillars, driven by the surface tension component during the collision. The directional rebound behavior is controlled by the droplet energy and the tilt angle. The micro/nanopillars demonstrate excellent self-cleaning property and mechanical durability, which shows the possibility of their practical engineering applications.

INTRODUCTION

The collision and contact process between water droplets and a solid surface is a dynamic physical phenomenon that occurs at the solid-liquid-gas interface between three phases (Wu et al., 2011). During the collision process, the contact wetting status between the water droplets and solid surface plays a dominant role in the applications of microfluidics, drug delivery, oil-water separation, anti-fog water collection, and printing (Liu et al., 2021; Lu et al., 2022; Mi et al., 2019; Whitesides, 2006; Yarin, 2006; Zhou et al., 2020; Wang et al., 2022a, 2022b). Nevertheless, the uncertainty of water droplet bounce limits its further development in these fields. In general, fluid behavior can be controlled by adjusting the related surface structure, but there are still challenges to overcome for progress to be made in novel engineering materials (Ishii et al., 2013).

Recently, it has been found that through surface micro/nanostructure or external field stimulation (An et al., 2021; Reyssat et al., 2009; Wang et al., 2018; Wu et al., 2020; Yang et al., 2018), in addition to the effective control of the transport of water droplets (Yada et al., 2022; Liu et al., 2014; Wang et al., 2016a, 2016b), the water droplets can be induced to spontaneously coalesce, merge, jump, and move in a certain direction (Liu et al., 2016; Shen et al., 2018; Timothée et al., 2017). For example, with the assistance of soft lithography, Lin et al. and Wang et al. (Lin et al., 2018; Wang et al., 2015) prepared a surface of magnetic micro/nanostructured arrays, which showed outstanding superhydrophobicity, and the long-distance nondestructive transport of water droplets was realized by regulating the external applied magnetic field. In addition, using a combination of soft lithography and crystal growth, Wang et al. (Wang et al., 2016a, 2016b) fabricated a superhydrophobic surface that could flexibly control the tilt angle of the microstructure, and thereby the directional rebound of water droplets was controlled by applying a magnetic field to regulate the tilt angle of the microstructure. Similarly, Li et al. (Li et al. (2021) also utilized a combination of soft lithography and crystal growth techniques to prepare microcone-structured array surfaces with different tilt angles. It was revealed that the as-obtained surfaces were superhydrophobic, and thus when water droplets collided with such surfaces, the water droplets rebounded directionally along the inclined direction of the microcones. In previous studies, the directional transport and rebound movement of water droplets were found to be mainly dependent on external stimuli or the design of the surface structure. However,

[1]Key Laboratory of Material Chemistry for Energy Conversion and Storage (Huazhong University of Science and Technology), Ministry of Education, Huazhong University of Science & Technology, Wuhan 430074, PR China

[2]Hubei Key Laboratory of Material Chemistry and Service Failure and Hubei Engineering Research Center for Biomaterials and Medical Protective Materials, Huazhong University of Science & Technology, Wuhan 430074, PR China

[3]School of Chemistry and Chemical Engineering, Huazhong University of Science & Technology, Wuhan 430074, PR China

[4]Kingfa Science and Technology Co., LTD., Guangzhou, Guangdong 510663, China

[5]Lead contact

*Correspondence: hengxie@hust.edu.cn (H.X.), jpqu@hust.edu.cn (J.-p.Q.)

https://doi.org/10.1016/j.isci.2022.105107

in the absence of any external stimulation, the mass production of directional water rebound material is still a tough issue, which in turn significantly hinders the exploration of the directional movement mechanisms of the rebound water droplets and limits the further application of directional water transport (Chu et al., 2020).

Under extreme environments, such as high temperature, high pressure, acidic, alkaline and salty conditions, polymer materials can maintain ideal physical and chemical stability and good mechanical strength (deLeon et al., 2016; Du et al., 2022; Gu et al., 2021). In addition, micro/nanostructures can be successfully constructed on the surface of thermoplastic polymers via molding, 3D printing, and injection molding and extrusion, which are characterized by their high efficiency and high accuracy (Liang et al., 2021; Xie et al., 2017, 2022; Bai et al., 2022; Park et al., 2022). For instance, Wu et al. (Wu et al. (2021) synthesized superhydrophobic polyethylene foam with a porosity of 98.6% via a combination of blending extrusion and modification methods. The as-prepared surface exhibited excellent water resistance and self-cleaning, in addition to anti-icing properties. Furthermore, Agapov et al. (Agapov et al. (2014) synthesized a surface of tilt nanopillars arrays by means of thermal growth and vapor deposition approaches. When water droplets with a Weber number (*We*) of $\geq$40 impacted on a surface at 325°C, a directional Leidenfrost effect was observed. Huang et al. (Huang and Wang, 2019) also designed a type of surface with a structure similar to that of a lotus leaf via an injection molding technique. It was found that the superhydrophobicity of the as-prepared surface was superior to the surface of a lotus leaf in terms of both dynamic stability and thermal persistence. Moreover, although the traditional molding process can be used to construct micro/nanostructures with excellent polymer surfaces to achieve various surface functions, including superhydrophobicity, anti-icing, and antibacterial properties (Kim et al., 2012; Mishchenko et al., 2010; He and Guo, 2021; Wang et al., 2021), how to construct polymer structures that exhibit the directional rebound of water droplets on their surfaces is still considered to be a huge challenge.

Accordingly, a hybrid method is proposed based on extrusion compression molding (Yang et al., 2021) and directional stretch demolding for the preparation of tilt micro/nanopillars on PP surfaces with directional water rebound property. Extrusion compression molding is a method that combines melt blending and polymer compression molding. This technology takes advantage of the dynamic elongational flow in an eccentric rotor extruder and the high-precise of compression molding for preparing the surface structures. As expected, the precision manufacturing of a polymer surface with tilt micropillars could be achieved via a combination of extrusion compression molding and directional stretch demolding, and thereby allowing continuous mass production to be achieved. Without any external stimulation, the as-prepared surface realized the directional movement of rebound water droplets, showing excellent wetting stability.

RESULTS AND DISCUSSION

Micromorphology of the PP surface

Figure 1 shows the morphologies of the mesh template, SiO_2 nanoparticles, and the tilt micropillars of the PP surface. As shown in Figure 1A, the mesh template is composed of interlaced steel wires with a transverse spacing, b_1, and longitudinal spacing, b_2, of 80 μm and 20 μm, respectively, and the width of the wire, b_3, is around 20 μm. The micromorphology of the SiO_2 nanoparticles is shown in Figure 1B, and these nanoparticles have a uniform size and mean diameter of 10–20 nm. Figure 1C shows the sample prepared under a stretch demolding rate of 20mm min^{-1} of the mesh screen. It is obvious that the surface of the sample is densely covered with a regular arrangement of tilt micropillars, and there is a slight tilt of ~5°, where the transverse spacing, b_4, the structural width, b_5, and longitudinal spacing, b_6, are ~100 μm, ~30 μm, and ~20 μm, respectively. When the temperature of the stretch demolding process is set to 130°C, the adhesive force between the mesh template and the PP matrix in a glassy state is small during the demolding process. Thus, during the demolding process, the microstructure is reasonably elongated and tilted along the direction of stretching, and eventually, the tilt micropillars are produced, as shown in Figure 1D. Importantly, the height and tilt angle of the surface microstructure can be controlled by the demolding temperature and the molding pressure. To improve the surface wetting stability of the tilt micro/nanopillars, tilt micro/nanopillars were prepared by SiO_2 modification, as shown in Figure 1E. As shown in Figure 1F, the surface of the tilt micropillars is fully covered by SiO_2 nanoparticles, and thereby such tilt micro/nanopillars with a tilt angle, θ_t, of 20° were generated. Figures 1G–2J shows the changes in the chemical composition of the material before and after modification. It is evident that Si and O are uniformly distributed on the surface of 130-PP@SiO_2, whereas the C element is dramatically reduced compared to that of the unmodified counterpart, indicating that SiO_2 nanoparticles are uniformly bonded on the surface of the tilt micropillars by the TEOS.

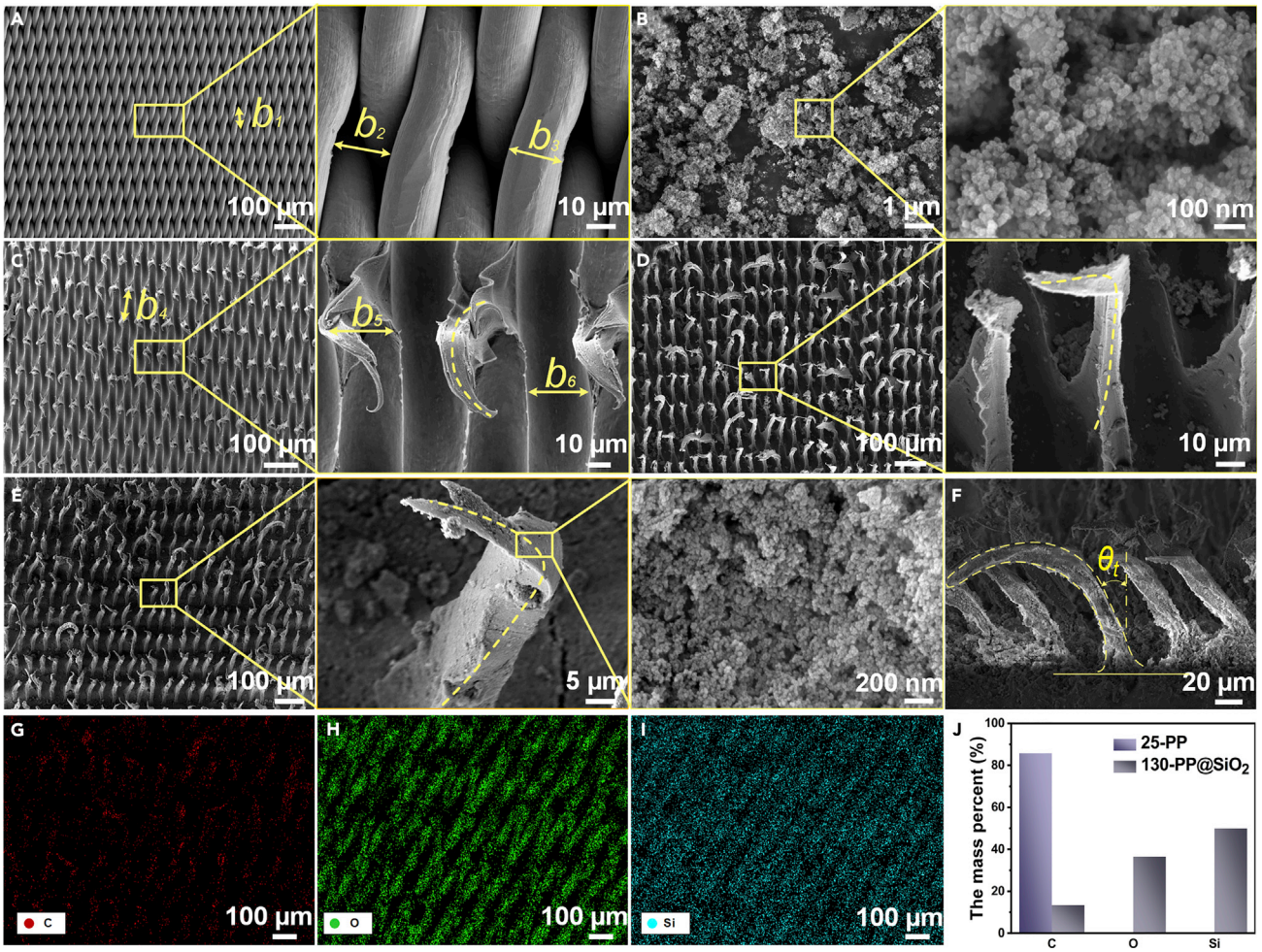

Figure 1. The surface micro-morphology and element composition

SEM images of (A) the screen mesh template, (B) SiO_2 nanoparticles, (C) 25-PP, (D) 130-PP, and (E and F) 130-PP@SiO_2. The distributions of (G) C, (H) O, and (I) Si on the surface of 130-PP@SiO_2, and (J) the elemental contents before and after modification.

Wetting behavior of the PP surface

Figure 2A shows the surface wetting states of the 25-PP, 130-PP, and 130-PP@SiO_2 samples, and the definitions of $RA_{//}$, $RA_{\perp 1}$, $RA_{\perp 2}$, and $RA_{\leftarrow}$ are given in Figure 2B. This demonstrates that the CA on the 25-PP surface increased from 95° ± 3° (related to Figure S1) to 146° ± 2°, and the values of $RA_{//}$, RA_1, and RA_2 are in the range of 21–25°, whereas the $RA_{\leftarrow}$ value is 36° ± 5°. By contrast, the CA of 130-PP surface is 151° ± 3°, and the values of $RA_{//}$, $RA_{\perp 1}$, and $RA_{\perp 2}$ are located in the range of 6–8°, whereas the value of $RA_{\leftarrow}$ is determined as 14° ± 4°. This suggests that when the temperature of demolding is increased, the water resistance of the sample is improved because of the increased height of the tilt micropillars, whereas the RA still shows anisotropy. The CA of the 130-PP@SiO_2 surface is 157° ± 3°, whereas the values of $RA_{//}$, $RA_{\perp 1}$ and $RA_{\perp 2}$ are decreased to the range of 3–4°, and $RA_{\leftarrow}$ is reduced to 9° ± 4°. As shown in Figure 2C, for the same sample surface, the values of $RA_{//}$, $RA_{\perp 1}$, and $RA_{\perp 2}$ are consistent, whereas the $RA_{\leftarrow}$ reached a maximum value. Owing to the directionality of the tilt micropillars, the water droplets encounter less resistance in the tilt direction and are confined in the opposite direction of the tilt micropillars (Cai et al., 2019). Therefore, the $RA_{//}$ is smaller than the $RA_{\leftarrow}$.

Directional rebound behavior of water droplets

Figure 3 shows a representative video screenshot of a water droplet with *We* value of 67.4 impacted the sample surface (related to Videos S1, S2, S3, and S4). When water droplets impacting the surfaces of

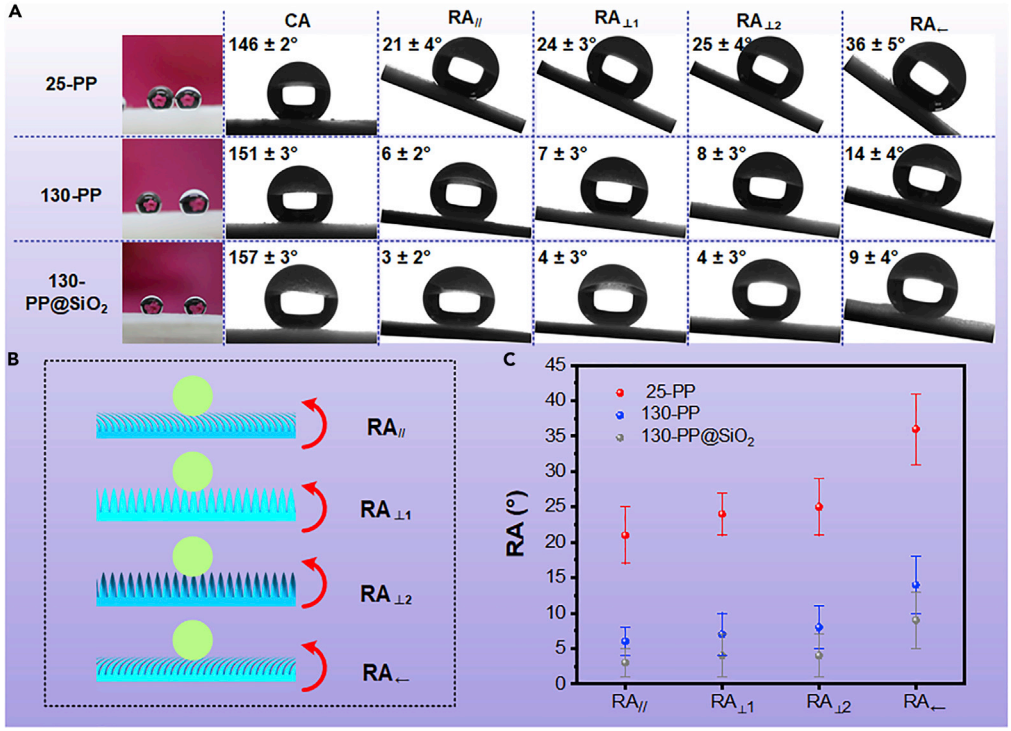

Figure 2. The surface wettability

(A) The surface wettability of 25-PP, 130-PP, and 130-PP@SiO_2 in the presence of water droplets of 5 μL, and (B) the testing directions of RA and (C) corresponding results.

25-PP and 130-PP, after 2.8 ms, the water droplets spread out to a maximum extent without any rebound, and then the related surface showed hydrophobic properties in its final state, compared with Figure S2. This phenomenon can be probably ascribed to the low height of the tilt micropillars, and thus the water droplets can infiltrate into the gap between adjacent micropillars, increasing the adhesion of such sample surface to the water droplets (Figures 3A and 3B). As the water droplet impacted the surface of the 130-PP@SiO_2 sample, it rebound to the highest point at 22.8 ms and showed hydrophobicity in its final state (Figure 3C). Of interest, the water droplets started to move toward the tilt direction of the micro/nanopillars during the rebound process, whereas the water droplet shifted to ~1.5 mm along the tilt direction relative to the original location in the final state. This indicates that the surface has the capacity to directionally transport the rebound water droplet, which is closely associated with the tilt micro/nanopillars. Furthermore, the shapes of the water droplet from the corresponding top views are shown in Figure 3D. It is apparent that after the water droplet impacted the 130-PP@SiO_2 surface, it rapidly spread out into a circular shape. In addition, there was a difference in the spreading distance between the left and right sides, with a b_7 value of 2.6 mm and a b_8 value of 2.8 mm. This can be explained by the fact that after contact the uneven force between the water droplet and the tilt micro/nanopillars led to differences in spreading speed, and ultimately the spreading distances are quite different. Subsequently, the retraction motion is also asymmetrical, with a b_9 value of 2.1 mm and a b_{10} value of 1.7 mm. This demonstrates that the water droplet moved toward the tilt direction of the micropillars, resulting in a deviation in the falling point.

To investigate the influence that different energies have on the rebound state of the water droplets, water droplets with *We* values of 20.2, 33.7, 47.2, 67.4, and 80.9 were used for surface impact, and the representative video screenshots (related to Videos S5, S6, S7, S8, and S9) are shown in Figures 4A–4E. The angle between the center and vertical lines of the rebound water droplet is defined as the takeoff deviation angle (α). The ratio of the maximum spreading diameter (D) to the original diameter (D_0) is defined as the spreading factor (D/D_0). The position where the water droplet first collides with the surface is defined as the first landing point, and the second landing point is located where the water droplet falls back on the surface of 130-PP@SiO_2 after rebounding to the highest position. The distance between the first and

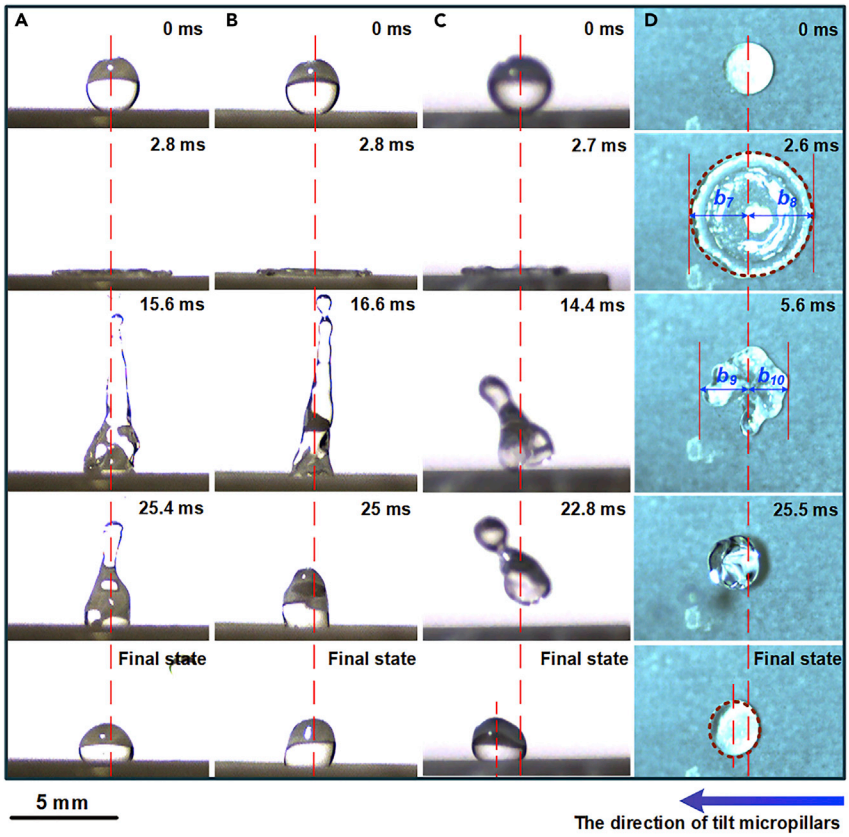

Figure 3. Representative screenshots of the impact process

Representative screenshots of the impact process on the (A) 25-PP, (B) 130-PP, and (C and D) 130-PP@SiO_2 surfaces.

second landing points is defined as the deviation distance (*L*). As shown in Figure 4A, when the *We* value of the water droplet is 20.2, the takeoff deviation angle is 2.7°, and the deviation distance, L_1 is 2.7 mm. However, when the *We* value increased to 33.7, the takeoff deviation angle increased, and L_2 is reduced to 0.5 mm. This is because during the rebound process, some of the energy is taken away by the separated water droplets as marked in the red circle, leading to a reduction in L_2 (Figure 4B). When the *We* value is continuously enhanced, the takeoff deviation angle further increased, and L_3 increased to 0.7 mm. As presented in Figure 4C, although the small separated water droplets can take away some of the energy, the deviation distance is also enhanced with the total energy increase. As shown in Figure 4D, when the *We* value reached 67.4, the takeoff deviation angle of the water droplet continued to be increased. After the water droplet rebounded to a certain height, it rotated around the centroid along the tilt micropillars orientation (ω_1), and the deviation distance L_4 also increased. When the *We* value is set as 80.9, the takeoff deviation angle reaches 21.1°. Owing to excessive energy, tiny water droplets can be separated at the moment of collision and take away more energy, leading to a further reduction in the deviation distance L_5. Nevertheless, the spin phenomenon of water droplets (ω_2) can be observed, as shown in Figure 4E, with the relevant deviation distances plotted in Figure 4F. This demonstrates that when the small water droplets were separated, the corresponding deviation distance increased with an increase in the *We* value in the order of $L_5 > L_3 > L_2$. In addition, the expansion factors and the takeoff deviation angles of the water droplets were enhanced with an increase in the *We* value (Figure 4G).

The expansion factor exhibits a linear relationship with the *We* value, which can be expressed using Equation (1):

$$y = 1.26 + 0.03x \quad \text{(Equation 1)}$$

Accordingly, this implies that the motion behavior of the water droplets can be controlled by regulating the *We* value.

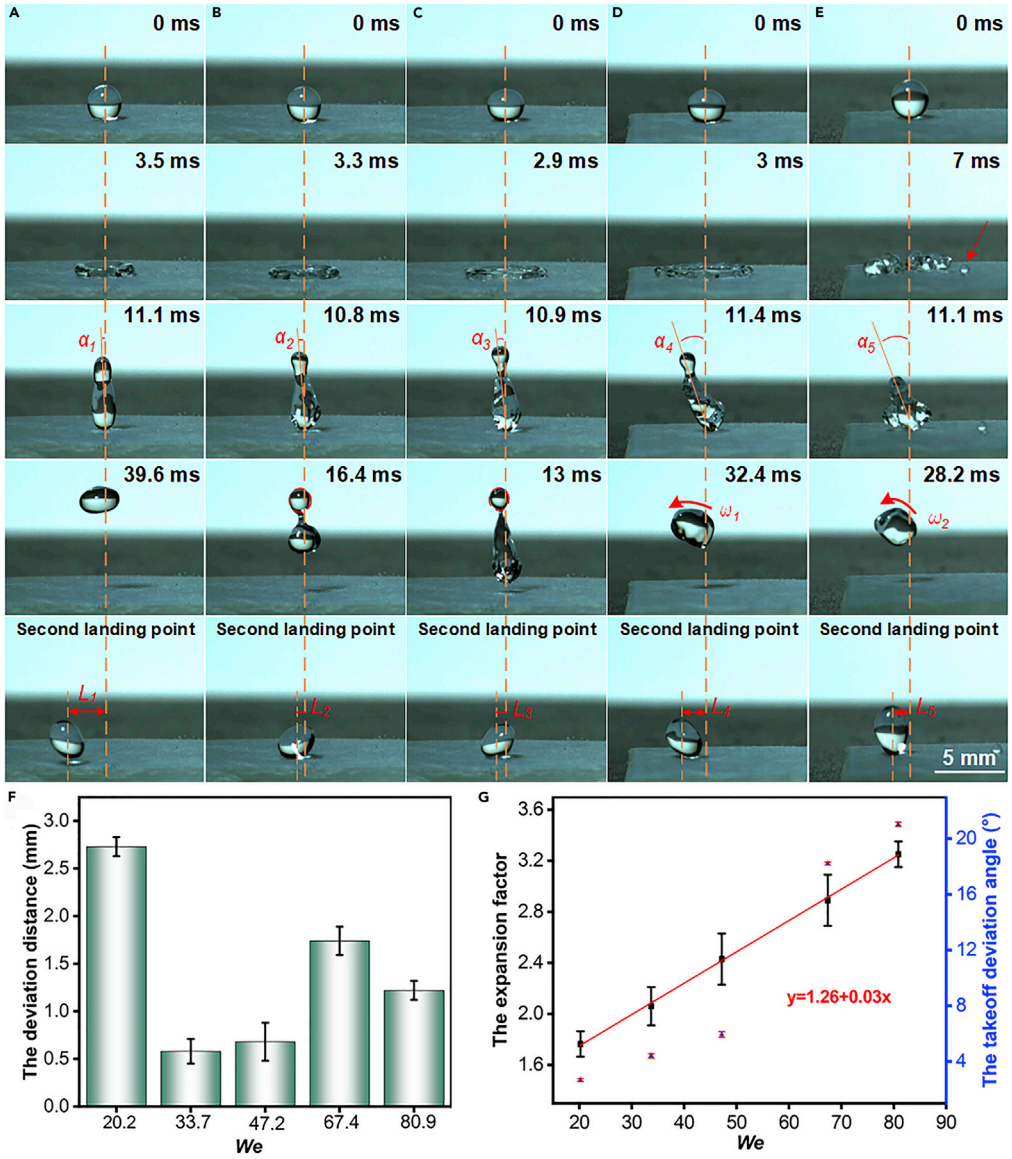

Figure 4. Representative screenshots of the impact process of water droplets with various *We* values

Representative video screenshots of the impact process of water droplets with various *We* values on the 130-PP@SiO_2 surface: (A) 20.2, (B) 33.7, (C) 47.2, (D) 67.4, and (E) 80.9; (F) The relationships of the expansion factor, the takeoff deviation angle, and *We* (G).

Movement regularity of rebound water droplets

Figures 5A–5E show video screenshots of a water droplet with a *We* value of 67.4 impacting the surface of 130-PP@SiO_2 at various tilt angles of −1°, −0.5°, 0°, 0.5° and 1°, respectively (related to Videos S10, S11, S8, S12, and S13). It can be observed that when the sample was rotated by −1° that the deviation direction of the water droplet was opposite the tilt direction of the micropillars. This is because the component force of gravity is larger than the guiding force, and has the opposite direction to the guiding force of the micropillars, and thereby the water droplet is shifted in the opposite direction (Figure 5A). When the sample was rotated by −0.5°, the tilt angle of the sample counteracted the guiding effect of the tilt micro/nanopillars, meaning that the water droplet did not deviate to the second landing point (Figure 5B). Without any rotation of the sample, there is a small takeoff deviation angle during the rebound process of the water droplet, and then the water droplet rebounded along the tilt direction of the micropillars (Figure 5C). When the sample is rotated by 0.5°, the takeoff deviation angle increases, but the separated water droplets take away part of

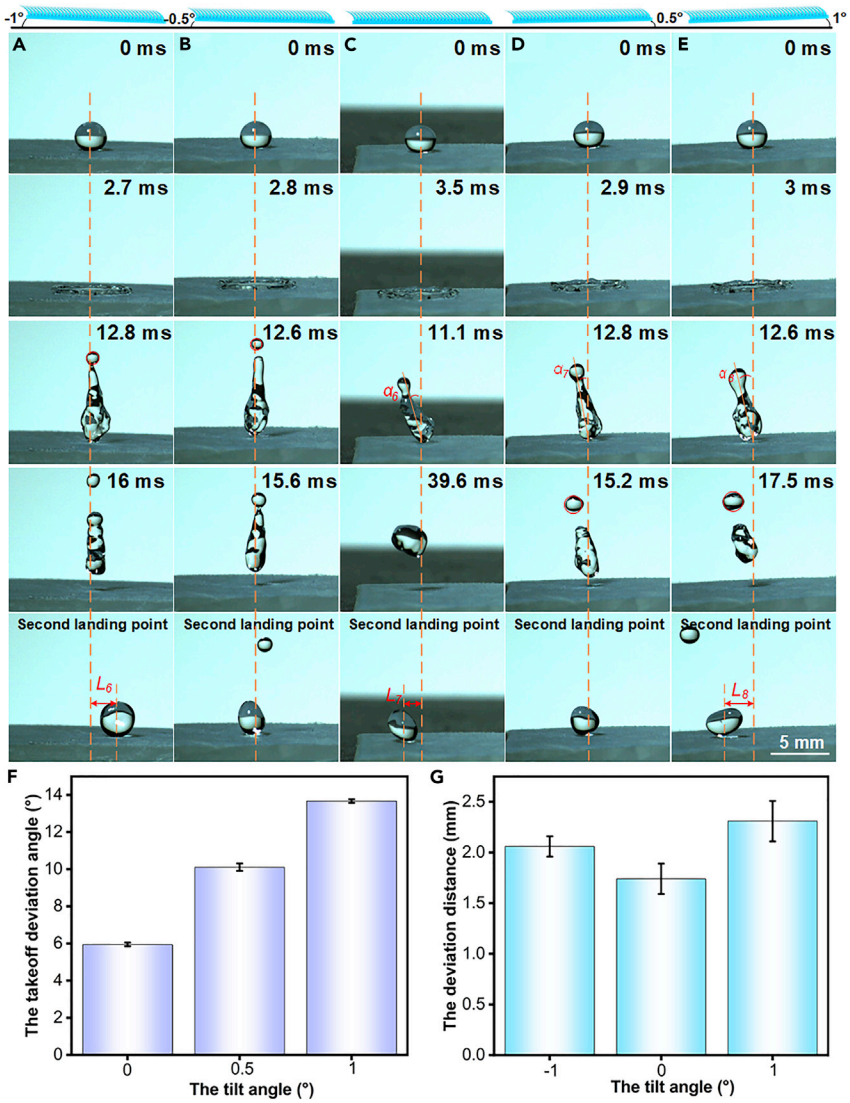

Figure 5. Representative screenshots of the impact process on the 130-PP@SiO_2 surface at different tilt angles

Representative screenshots of the impact process on the 130-PP@SiO_2 surface at tilt angles of (A) −1°, (B) −0.5°, (C) 0°, (D) 0.5°, and (E) 1°, respectively, (F) relationship of the tilt angle and the takeoff deviation angle, and (G) the relationship of the tilt angle and the deviation distance.

the energy, resulting in no deviation at the second landing point (Figure 5D). The takeoff deviation angle of the water droplet increases when the tilt angle of the surface increases (Figure 5E). In addition, the takeoff deviation angle and deviation distance of water droplets impacted surfaces with different tilt angles are presented in Figures 5F and 5G, respectively. When the tilt direction of the sample is consistent with that of the micropillars, the increased tilt angle of the sample can also bring about an enhancement in the takeoff deviation angle of the water droplet. This is because the component force of gravity equals the guiding force of micropillars, causing the takeoff deviation angle to increase (Figure 5F). When the tilt angle of the sample increased, the deviation distance of the water droplet is increased, indicating that the force of the tilt surface imposed on the water droplet is larger than the guiding force of the micropillars (Figure 5G). Herein, the motion of the water droplets could be controlled by adjusting the tilt angle of 130-PP@SiO_2.

Motion mechanism analysis of directional rebound

When a water droplet impacts a superhydrophobic surface, the resultant rebound trajectory is closely related to the surface structure (Liu et al., 2020; Mi et al., 2017). To reveal the mechanism of motion that the tilt

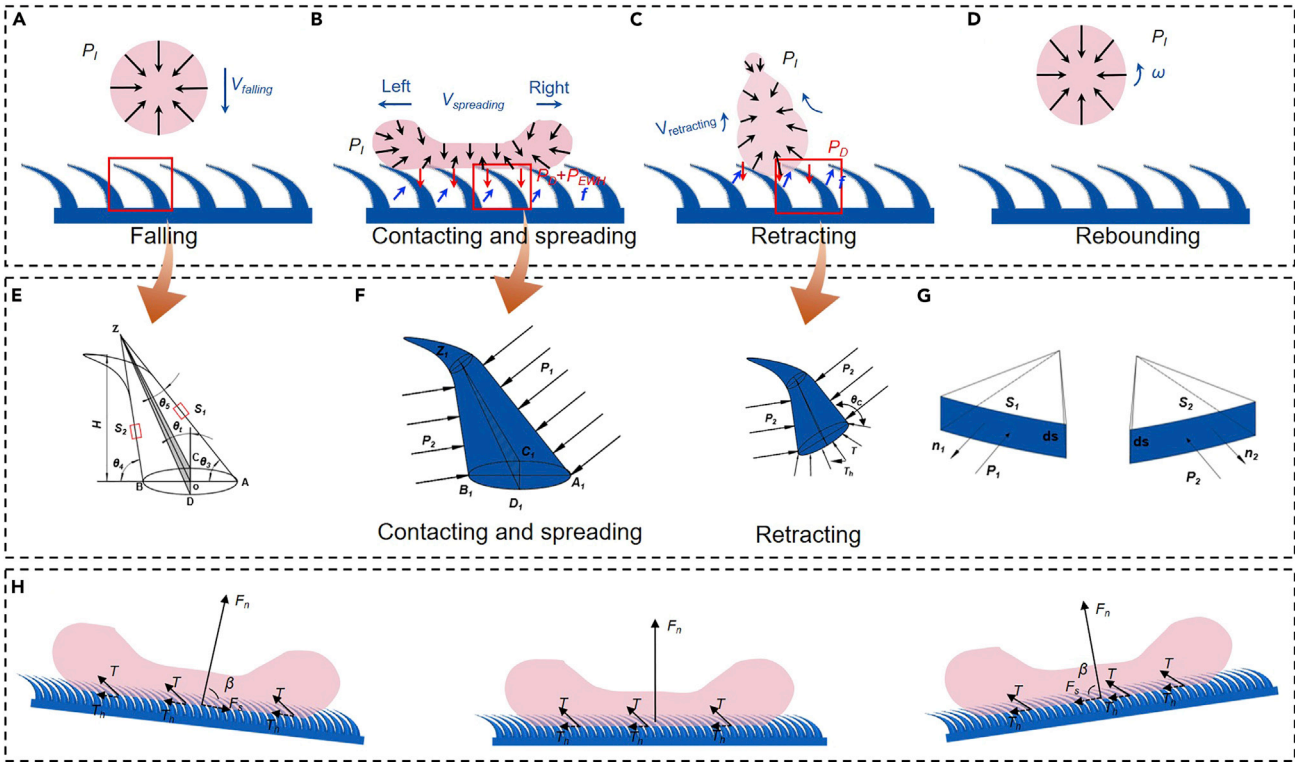

Figure 6. The mechanical models of water droplets impacting tilt surface

(A–D) States of water droplets impacting the micro/nanopillars surface, (E) model of the tilt micro/nanopillars, in which *H* represents the height of the micropillar and the cross-sectional morphology of the root of the tilt micro/nanopillars is identified as elliptical ACBD, (F) force model of water droplets in contact with tilt micro/nanopillars, (G) schematic diagram of the unit normal vectors, n_1 and n_2, in the left and right regions, respectively, and (H) mechanical models of water droplets impacting tilt surface.

micro/nanopillars impose on the rebound water droplet, the falling and rebounding process of the water droplet can be roughly divided into several parts, as illustrated in Figures 6A–6D. During this process, the tilt micro/nanopillars can be simplified to the model shown in Figure 6E. During the contact process between the water droplet and the surface, the stress state of the tilt micro/nanopillars is given in Figure 6F.

As shown in Figure 6A, when the water droplet fell freely, it remained spherical because of the cohesion between the water molecules, P_I, and the surface tension, T. When water droplets impact the surface of the tilt micro/nanopillars, they are subjected to the dynamic pressure, P_D, and effective water hammer pressure, P_{EWH}. Moreover, during the spreading and retracting process, the water droplets are subjected to the force, f, exerted by the micropillars, and the distribution of the corresponding force, f, is presented in Figures 6B and 6C.

With regard to the axial section $Z_1C_1D_1$ (Figure 6F), a micropillar can be divided into left and right regions. The pressures in the left and right regions of the micropillar are defined as P_2 and P_1, respectively. Therefore, the resultant force f can be calculated using the following Equation (2):

$$f = \iint_{S_1} P_1 ds \cos\theta_1 - \iint_{S_2} P_2 ds \cos\theta_2 \qquad \text{(Equation 2)}$$

where θ_1 is denoted as the angle between the normal vectors, n_1, and the $Z_1A_1B_1$ plane, and θ_2 represents the angle between the normal vectors, n_2, and the $Z_1A_1B_1$ plane (Figure 6G).

When $S_1 > S_2$, the relation of $P_1 > P_2$ can be obtained, and the resultant force is perpendicular to the right region of the micropillar, thus f can also be estimated from the following Equation (3):

$$f = \frac{\Delta m v_t - \Delta m v \cos\theta_3}{t} \quad \text{(Equation 3)}$$

where v_t is identified as the velocity along the normal line of the right region of the micropillar, t is the contact time, Δm is the mass of the water droplet making contact with each micropillar, and θ_3 and θ_4 are the angles between the bottom surface and the micropillar (Figure 6E), where θ_3 and θ_4 can be calculated using the following Equations (4) and (5):

$$\theta_3 = \pi/2 - \theta_5 - \theta_t \quad \text{(Equation 4)}$$

$$\theta_4 = \pi/2 + \theta_5 - \theta_t \quad \text{(Equation 5)}$$

where θ_5 is defined as the half apex angle of the axial section of the micropillar. According to Equation (3), when the water droplet impacts the surface, the resultant force f of each micropillar on water droplets cannot be zero. Simultaneously, the water droplet is subjected to a force f_1 opposite to the direction of the micropillar, and it can be calculated by Equation (6):

$$f_1 = nf\sin\theta_3 = n\frac{\Delta m v_t - \Delta m v\cos\theta_3}{t}\sin\theta_3 \quad \text{(Equation 6)}$$

where n is defined as the number of water droplets contacting the micropillar. When the water droplet vertically impacts a smooth hydrophobic surface, the force imposed on the water droplet is uniformly symmetrical, and the water droplet can spread out in all directions at the same speed. However, when impacting the tilt micro/nanopillars surface, the water droplet is affected by the force (f_1) opposite to the micropillar. As shown in Figure 6B, the spreading speed of the water droplet along the tilt direction of the micropillar was slower than that along the opposite direction. Accordingly, the spreading distance along the tilt direction of the micropillar is also shorter than that along the opposite direction. During the spreading process, the spreading speed ($V_{spreading}$) of the water droplets gradually decreased to 0, whereas the corresponding expansion factor (D/D_0) reached a maximum value.

The water droplet begins to shrink after spreading to a maximum extent, in which the pressure load remained in balance, and both the v and We value of water droplets are determined to be zero. However, the surface tension is unbalanced. When the contact surface is set as a circle, the resultant force T driven by the surface tension can be evaluated by Equation (7):

$$T = n\gamma l\cos(\theta_c - \theta_5) = 2n\pi\gamma r\cos(\theta_c - \theta_5) \quad \text{(Equation 7)}$$

where l is the length of the contact line, r is the radius of the contact surface, and θ_c is the CA. The resultant force can be upward along the axis of the micropillar (Figure 6F) so that the water droplet has a component forth T_h along the tilt direction of the micropillar, which can be determined by the following Equation (8):

$$T_h = T\sin\theta_t \quad \text{(Equation 8)}$$

Eventually, as shown in Figure 6C, the surface tension of water droplets is unbalanced when it impacts on the tilt micropillars. The water droplet rebound from the micro/nanopillars surface with a angular velocity (ω) under the action of T_h (Figure 6C), resulting in a certain deviation distance (L), (Figure 6D).

According to Equations (7) and (8), when the water droplet bounced and the separation of tiny water droplets could not be detected, i.e., $L, \omega, \alpha \propto T_h$, $T_h \propto T$, and $T \propto n$, the relationship of $L, \omega, \alpha \propto n$ can be determined. Therefore, with an increase in We value, the spreading area of the water droplet increased, and the number of contact micropillars also increased, which can bring about an improvement in the takeoff deviation angle and deviation distance.

When the water droplet impacts the tilt surface, it is subjected to the reaction force F_n induced by the surface, and the direction of F_n is perpendicular to the surface upward, as shown in Figure 6H. When the rotation angle is negative, the reaction force F_n performed on the water droplet can have a component F_s along the parallel direction of the tilt plane, which is opposite to the micropillar force T_h, leading to a reduced deviation distance. If the rotation angle is beyond a critical value, there is a deviation distance opposite the tilt direction of the micropillar. When the rotation angle is set as zero, the water droplet is only affected by the action of T_h. When the rotation angle is set as a negative value, the deviation distance is increased. By contrast, when the rotation angle is set as a positive value, F_s is consistent with T_h, leading to a further enhancement in deviation distance.

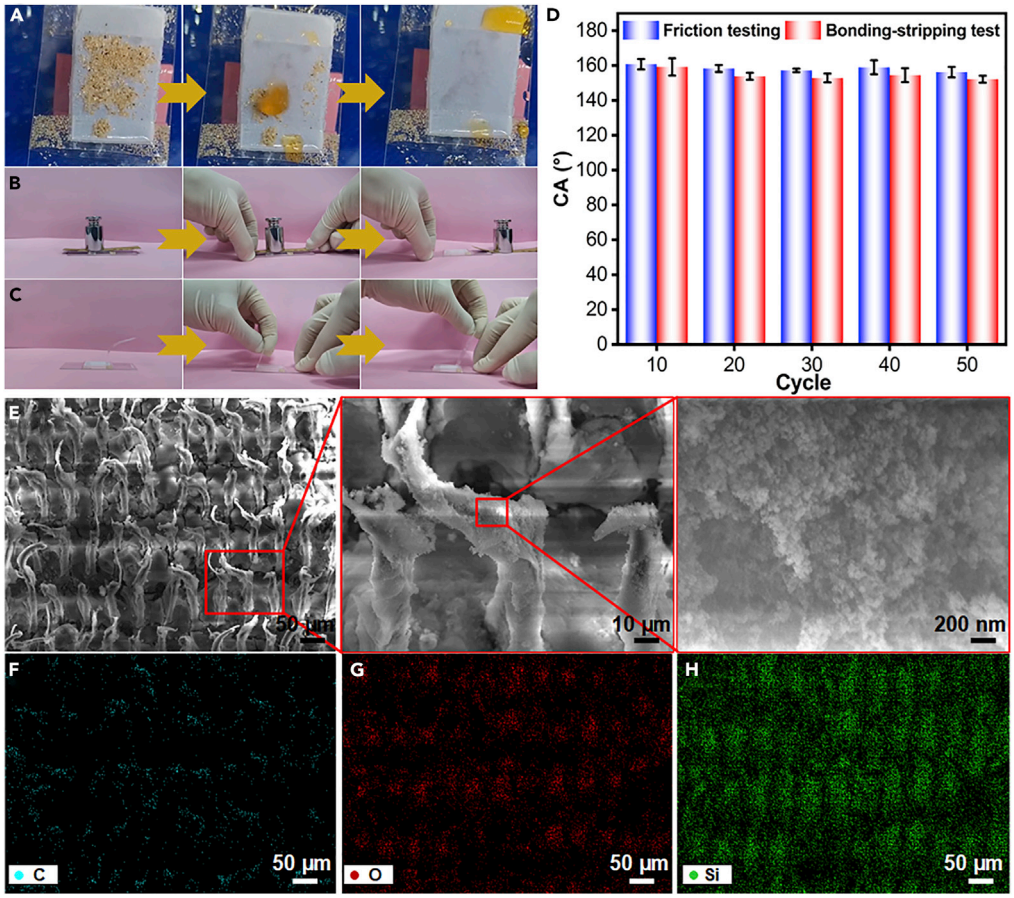

Figure 7. Self-cleaning testing and friction testing of the 130-PP@SiO_2 surface

(A) Self-cleaning testing of the 130-PP@SiO_2 surface, (B) friction testing of the 130-PP@SiO_2 surface, (C) bonding-stripping testing of the 130-PP@SiO_2 surface using adhesive tape, (D) relationship of surface wettability and friction/bonding-stripping cycles, (E) SEM images of after 50 cycles of friction/bonding-stripping and the corresponding elemental distributions of (F) C, (G) O, and (H) Si.

Durability of tilt micro/nanopillars

Figure 7A shows that the yellow water droplet is favorable for taking away the pollutants on the surface of the sample, and there is no residual yellow water droplet, indicating that the sample has excellent self-cleaning performance. Generally, the durability of the superhydrophobic surface is crucial to its engineering application (Varughese and Bhandaru, 2020; Ma et al., 2021; Xie et al., 2021). To investigate the durability of tilt micro/nanopillars, the 2000# (45 × 10 mm) abrasive paper with 100 g weight on the surface was applied and subjected to friction testing in a single friction length of 45 mm (Figure 7B). Furthermore, the adhesive tape was used to conduct bonding-stripping testing on the surface (Figure 7C). Figure 7D shows the CA for every 10 friction/bonding-stripping cycles. The surface still remains in a superhydrophobic state, suggesting that the tilt micro/nanopillars can effectively prevent the infiltration of water droplets. The tilt micro/nanopillars have sufficient stability and durability for working in harsh environments. As shown in Figure 7E, the tilt micro/nanopillars are reserved on the surface after the durability testing. As shown in Figures 7F–7H, the Si element is reduced by 31.3% after the friction/bonding-stripping tests (related to Figure S2). This means some SiO_2 was taken away after 50 friction/bonding-stripping cycles, and the partial hydrolyzing of TEOS provides enough bonding strength between the PP matrix and SiO_2. Therefore, the tilt micro/nanopillars on the surface show sufficient robustness.

Conclusions

A PP surface with tilt micro/nanopillars is efficiently fabricated via the extrusion compression molding and directional stretch demolding method. The tilt micro/nanopillars endowed the PP surface with excellent water

repellency and differentiated RA. The value of $RA_{\leftarrow}$ ($9 \pm 4°$), which is opposite the tilt direction of the micro/nanopillars, was the highest. There is an obvious directional rebound when water droplets impacted the surface, which is mainly because the water droplets are guided to rebound along the tilt direction of the micro/nanopillars by the surface tension component. The takeoff deviation angle and rebound path could be adjusted by controlling the *We* value of the water droplets and the tilt angle of the surface. Furthermore, repeated friction and bonding-stripping testing were found to inflict little damage on the tilt micro/nanopillars and the PP surface still maintained excellent water repellency. The proposed method provides an ideal candidate for the efficient fabrication of tilt micro/nanopillars for directing the motion of dynamic water droplet.

Limitations of the study

Integration of the extrusion compression molding with directional stretch demolding method is one of the first attempts to prepare the tilt micro/nanopillars surface. This study describes the directional rebound of water droplets on the tilt micro/nanopillars surface and tilt surface. Although this study showed that water droplets can directional rebound when they impacted the tilt micro/nanopillars surface, the precise control of the takeoff deviation angle and deviation distance of water droplets was not achieved. Analysis and optimization between structural parameters (e.g., altering the tilt angle of the micro/nanopillar and the number of pillar) and the directional rebound of the water droplet could further improve the precise control of the takeoff deviation angle and deviation distance. Furthermore, studying the collision process of water droplets on the tilt micro/nanopillars surface would be of great significance in the fields of water droplet potential energy capture and microfluidic.

STAR★METHODS

Detailed methods are provided in the online version of this paper and include the following:

- KEY RESOURCES TABLE
- RESOURCE AVAILABILITY
  - Lead contact
  - Materials availability
  - Data and code availability
- EXPERIMENTAL MODEL AND SUBJECT DETAILS
  - Preparation of tilt micro/nanopillars on the PP surface
  - Characterization
- QUANTIFICATION AND STATISTICAL ANALYSIS

SUPPLEMENTAL INFORMATION

Supplemental information can be found online at https://doi.org/10.1016/j.isci.2022.105107.

ACKNOWLEDGMENTS

We acknowledge the National Natural Science Foundation of China (Grant No. 52103031 and 52073107), the National Key Research and Development Program of China (Grant No. 2020YFB1709304), the Opening Project of Guangdong Provincial Key Laboratory of Technique and Equipment for Macromolecular Advanced Manufacturing, South China University of Technology, China (Grant No. 2021kfkt05) and the Fundametal Research Funds for the Central Universites, Huazhong University of Science and Technology, China (YCJJ202203002).

AUTHOR CONTRIBUTIONS

Y. D.: Data curation, formal analysis, methodology, Writing - Original draft. T.W.: Reviewing and Editing, formal analysis, and investigation. X.L.L.: Drawing and investigation. W.L.Z.: Drawing and experiment. C.D.: Data curation and methodology. Y.Q.Y.: Formal analysis. J.G.W.: Software. X. L.: Methodology. H.X.: Funding acquisition, Writing – Review and editing, Supervision, Project administration. J.P.Q.: Funding acquisition, validation, and resources.

DECLARATION OF INTERESTS

The authors declare no competing interests.

INCLUSION AND DIVERSITY

We support inclusive, diverse, and equitable conduct of research.

Received: June 21, 2022
Revised: August 24, 2022
Accepted: September 7, 2022
Published: October 21, 2022

REFERENCES

Agapov, R.L., Boreyko, J.B., Briggs, D.P., Srijanto, B.R., Retterer, S.T., Collier, C.P., and Lavrik, N.V. (2014). Asymmetric wettability of nanostructures directs leidenfrost droplets. ACS Nano *8*, 860–867. https://doi.org/10.1021/nn405585m.

An, Q., Wang, J., Zhao, F., Li, P., and Wang, L. (2021). Unidirectional water transport on a two-dimensional hydrophilic channel with anisotropic superhydrophobic barriers. Soft Matter *17*, 8153–8159. https://doi.org/10.1039/D1SM00697E.

Bai, X., Gai, C., Wu, D., Zhu, J., Wu, G., Zhang, M., Liu, Y., Sun, J., Zhuang, J., Huang, Y., and Xu, H. (2022). Intelligent sensing system of the car seat with flexible piezoresistive sensor of double-layer conductive network. IEEE Sens. J. *22*, 3113–3121. https://doi.org/10.1109/JSEN.2022.3142081.

Cai, Y., Luo, X., Tian, Y., Murad Hasan, R.M., Chang, W., and Qin, Y. (2019). Dynamic behaviours of water droplets impacting on laser ablated surfaces. Colloids Surf. A Physicochem. Eng. Asp. *580*, 123743. https://doi.org/10.1016/j.colsurfa.2019.123743.

Chu, Z., Jiao, W., Huang, Y., Chen, L., Zheng, Y., Wang, R., and He, X. (2020). Directional rebound control of droplets on low-temperature regular and irregular wrinkled superhydrophobic surfaces. Appl. Surf. Sci. *530*, 147099. https://doi.org/10.1016/j.apsusc.2020.147099.

de Leon, A.C., Chen, Q., Palaganas, N.B., Palaganas, J.O., Manapat, J., and Advincula, R.C. (2016). High performance polymer nanocomposites for additive manufacturing applications. React. Funct. Polym. *103*, 141–155. https://doi.org/10.1016/j.reactfunctpolym.2016.04.010.

Du, Y., Wu, T., Xie, H., and Qu, J.P. (2022). One-step laser etching of a bionic hierarchical structure on a silicone rubber surface with thermal and acid/alkali resistance and tunable wettability. Soft Matter *18*, 3412–3421. https://doi.org/10.1039/D2SM00242F.

Gu, H., Gao, C., Zhou, X., Du, A., Naik, N., and Guo, Z. (2021). Nanocellulose nanocomposite aerogel towards efficient oil and organic solvent adsorption. Adv. Compos. Hybrid Mater. *4*, 459–468. https://doi.org/10.1007/s42114-021-00289-y.

He, H., and Guo, Z. (2021). Superhydrophobic materials used for anti-icing theory, application, and development. iScience *24*, 103357. https://doi.org/10.1016/j.isci.2021.103357.

Huang, H.X., and Wang, X. (2019). Biomimetic fabrication of micro-/nanostructure on polypropylene surfaces with high dynamic superhydrophobic stability. Mater. Today Commun. *19*, 487–494. https://doi.org/10.1016/j.mtcomm.2019.04.005.

Ishii, D., Horiguchi, H., Hirai, Y., Yabu, H., Matsuo, Y., Ijiro, K., Tsujii, K., Shimozawa, T., Hariyama, T., and Shimomura, M. (2013). Water transport mechanism through open capillaries analyzed by direct surface modifications on biological surfaces. Sci. Rep. *3*, 3024. https://doi.org/10.1038/srep03024.

Kim, P., Wong, T.S., Alvarenga, J., Kreder, M.J., Adorno-Martinez, W.E., and Aizenberg, J. (2012). Liquid-infused nanostructured surfaces with extreme anti-ice and anti-frost performance. ACS Nano *6*, 6569–6577. https://doi.org/10.1021/nn302310q.

Li, P., Xu, X., Yu, Y., Wang, L., and Ji, B. (2021). Biased motions of a droplet on the inclined micro-conical superhydrophobic surface. ACS Appl. Mater. Interfaces *13*, 27687–27695. https://doi.org/10.1021/acsami.1c07209.

Liang, X., Liu, Y., Liu, Z., Ma, J., Zhang, Z., Ruan, W., Ren, S., Peng, T., Wu, X., and Shi, H. (2021). Ultrasonic injection molding of glass fiber reinforced polypropylene parts using tungsten carbide-cobalt mold core. Mater. Des. *205*, 109771. https://doi.org/10.1016/j.matdes.2021.109771.

Lin, Y., Hu, Z., Zhang, M., Xu, T., Feng, S., Jiang, L., and Zheng, Y. (2018). Magnetically induced low adhesive direction of nano/micropillar arrays for microdroplet transport. Adv. Funct. Mater. *28*, 1800163. https://doi.org/10.1002/adfm.201800163.

Liu, C., Ju, J., Ma, J., Zheng, Y., and Jiang, L. (2014). Directional drop transport achieved on high-temperature anisotropic wetting surfaces. Adv. Mater. *26*, 6086–6091. https://doi.org/10.1002/adma.201401985.

Liu, C., Liu, Q., and Lin, Z. (2020). Dynamical behavior of droplets transiently impacting on superhydrophobic microstructures. Phys. Fluids *32*, 103304. https://doi.org/10.1063/5.0024400.

Liu, J., Guo, H., Zhang, B., Qiao, S., Shao, M., Zhang, X., Feng, X.Q., Li, Q., Song, Y., Jiang, L., and Wang, J. (2016). Guided self-propelled leaping of droplets on a micro-anisotropic superhydrophobic surface. Angew. Chem. Int. Ed. Engl. *55*, 4265–4269. https://doi.org/10.1002/anie.201600224.

Liu, X., Trosseille, J., Mongruel, A., Marty, F., Basset, P., Laurent, J., Royon, L., Cui, T., Beysens, D., and Bourouina, T. (2021). Tailoring silicon for dew water harvesting panels. iScience *24*, 102814. https://doi.org/10.1016/j.isci.2021.102814.

Lu, H., Shi, W., Guo, Y., Guan, W., Lei, C., and Yu, G. (2022). Materials engineering for atmospheric water harvesting: progress and perspectives. Adv. Mater. *34*, e2110079. https://doi.org/10.1002/adma.202110079.

Ma, J., Porath, L.E., Haque, M.F., Sett, S., Rabbi, K.F., Nam, S., Miljkovic, N., and Evans, C.M. (2021). Ultra-thin self-healing vitrimer coatings for durable hydrophobicity. Nat. Commun. *12*, 5210. https://doi.org/10.1038/s41467-021-25508-4.

Mi, H.Y., Jing, X., Huang, H.X., and Turng, L.S. (2017). Controlling superwettability by microstructure and surface energy manipulation on three-dimensional substrates for versatile gravity driven oil/water separation. ACS Appl. Mater. Interfaces *9*, 37529–37535. https://doi.org/10.1021/acsami.7b10901.

Mi, H.Y., Jing, X., Liu, Y., Li, L., Li, H., Peng, X.F., and Zhou, H. (2019). Highly durable superhydrophobic polymer foams fabricated by extrusion and supercritical CO2 foaming for selective oil absorption. ACS Appl. Mater. Interfaces *11*, 7479–7487. https://doi.org/10.1021/acsami.8b21858.

Mishchenko, L., Hatton, B., Bahadur, V., Taylor, J.A., Krupenkin, T., and Aizenberg, J. (2010). Design of ice-free nanostructured surfaces based on repulsion of impacting water droplets. ACS Nano *4*, 7699–7707. https://doi.org/10.1021/nn102557p.

Park, S., Shou, W., Makatura, L., Matusik, W., and Fu, K.K. (2022). 3D printing of polymer composites: materials, processes, and applications. Matter *5*, 43–76. https://doi.org/10.1016/j.matt.2021.10.018.

Reyssat, M., Pardo, F., and Quéré, D. (2009). Drops onto gradients of texture. Europhys. Lett. *87*, 36003. https://doi.org/10.1209/0295-5075/87/36003.

Shen, Y., Xie, Y., Tao, J., Chen, H., Zhu, C., Jin, M., and Lu, Y. (2018). Rationally designed nanostructure features on superhydrophobic surfaces for enhancing self-propelling dynamics of condensed droplets. ACS Sustain. Chem. Eng. *7*, 2702–2708. https://doi.org/10.1021/acssuschemeng.8b05780.

Mouterde, T., Lehoucq, G., Xavier, S., Checco, A., Black, C.T., Rahman, A., Midavaine, T., Clanet, C., and Quéré, D. (2017). Antifogging abilities of model nanotextures. Nat. Mater. *16*, 658–663. https://doi.org/10.1038/NMAT4868.

Varughese, S.M., and Bhandaru, N. (2020). Durability of submerged hydrophobic surfaces.

Soft Matter *16*, 1692–1701. https://doi.org/10.1039/C9SM01942A.

Wang, J.N., Liu, Y.Q., Zhang, Y.L., Feng, J., and Sun, H.B. (2018). Pneumatic smart surfaces with rapidly switchable dominant and latent superhydrophobicity. NPG Asia Mater. *10*, e470. https://doi.org/10.1038/am.2017.218.

Wang, L., Gao, C., Hou, Y., Zheng, Y., and Jiang, L. (2016a). Magnetic field-guided directional rebound of a droplet on a superhydrophobic flexible needle surface. J. Mater. Chem. *4*, 18289–18293. https://doi.org/10.1039/C6TA08333A.

Wang, L., He, Z., Ding, Y., Zhou, X., and Liu, J. (2016b). The rebound motion of liquid metal droplet on flexible micro/nano needle forest. Adv. Mater. Interfaces *3*, 1600008. https://doi.org/10.1002/admi.201600008.

Wang, L., Zhang, M., Shi, W., Hou, Y., Liu, C., Feng, S., Guo, Z., and Zheng, Y. (2015). Dynamic magnetic responsive wall array with droplet shedding-off properties. Sci. Rep. *5*, 11209. https://doi.org/10.1038/srep11209.

Wang, T., Xing, L., Qu, M., Pan, Y., Liu, C., Shen, C., and Liu, X. (2022a). Superhydrophobic polycarbonate blend monolith with micro/nano porous structure for selective oil/water separation. Polymer *253*, 124994. https://doi.org/10.1016/j.polymer.2022.124994.

Wang, T., Lu, Z., Wang, X., Zhang, Z., Zhang, Q., Yan, B., and Wang, Y. (2021). A compound of ZnO/PDMS with photocatalytic, self-cleaning and antibacterial properties prepared via two-step method. Appl. Surf. Sci. *550*, 149286. https://doi.org/10.1016/j.apsusc.2021.149286.

Wang, X., Zhang, M., Schubert, D.W., and Liu, X. (2022b). Oil-Water separation polypropylene foam with advanced solvent-evaporation induced coexistence of microspheres and microporous structure. Macromol. Rapid Commun. *43*, 2200177. https://doi.org/10.1002/marc.202200177.

Whitesides, G.M. (2006). The origins and the future of microfluidics. Nature *442*, 368–373. https://doi.org/10.1038/nature05058.

Wu, J., Ma, R., Wang, Z., and Yao, S. (2011). Do droplets always move following thewettability gradient? Appl. Phys. Lett. *98*, 204104. https://doi.org/10.1063/1.3592997.

Wu, J., Yin, K., Li, M., Wu, Z., Xiao, S., Wang, H., Duan, J.A., and He, J. (2020). Under-oil self-driven and directional transport of water on a femtosecond laser-processed superhydrophilic geometry-gradient structure. Nanoscale *12*, 4077–4084. https://doi.org/10.1039/C9NR09902F.

Wu, T., Xu, W.H., Guo, K., Xie, H., and Qu, J.P. (2021). Efficient fabrication of lightweight polyethylene foam with robust and durable superhydrophobicity for self-cleaning and anti-icing applications. Chem. Eng. J. *407*, 127100. https://doi.org/10.1016/j.cej.2020.127100.

Xie, H., Huang, H.X., and Peng, Y.J. (2017). Rapid fabrication of bio-inspired nanostructure with hydrophobicity and antireflectivity on polystyrene surface replicating from cicada wings. Nanoscale *9*, 11951–11958. https://doi.org/10.1039/C7NR04176D.

Xie, H., Xu, W.H., Du, Y., Gong, J., Niu, R., Wu, T., and Qu, J.P. (2022). Cost-effective fabrication of micro-nanostructured superhydrophobic polyethylene/graphene foam with self-floating, optical trapping, acid-/alkali resistance for efficient photothermal deicing and interfacial evaporation. Small *18*, 2200175. https://doi.org/10.1002/smll.202200175.

Xie, H., Xu, W.H., Fang, C., and Wu, T. (2021). Efficient and economical approach for flexible photothermal icephobic copper mesh with robust superhydrophobicity and active deicing property. Soft Matter *17*, 1901–1911. https://doi.org/10.1039/D0SM01930E.

Yada, S., Lacis, U., Wijngaart, W.V.D., Lundell, F., Amberg, G., and Bagheri, S. (2022). Droplet impact on asymmetric hydrophobic microstructures. https://doi.org/10.48550/arXiv.2203.04627.

Yang, L., Sheng, X.D., Yang, Q., Liu, J.Q., Wu, W.J., Li, D.Y., Du, J.H., Zhang, B., and Fan, S.Q. (2021). Fabrication of biomimetic anisotropic super-hydrophobic surface with rice leaf-like structures by femtosecond laser. Opt. Mater. *112*, 110740. https://doi.org/10.1016/j.optmat.2020.110740.

Yang, Z., Park, J.K., and Kim, S. (2018). Magnetically responsive elastomer-silicon hybrid surfaces for fluid and light manipulation. Small *14*, 1702839. https://doi.org/10.1002/smll.201702839.

Yarin, A.L. (2006). Drop impact dynamics: splashing, spreading, receding, bouncing. Annu. Rev. Fluid Mech. *38*, 159–192. https://doi.org/10.1146/annurev.fluid.38.050304.092144.

Zhou, Y., Huang, S., and Tian, X. (2020). Magnetoresponsive surfaces for manipulation of nonmagnetic liquids: design and applications. Adv. Funct. Mater. *30*, 1906507. https://doi.org/10.1002/adfm.201906507.

STAR★METHODS

KEY RESOURCES TABLE

REAGENT or RESOURCE	SOURCE	IDENTIFIER
Polypropylene (PP), Fujian Zhongjing Petrochemical Co., Ltd., China, T30S.		
Nano silica particles (SiO_2), Evonik Industries AG, Germany, R974.		
Electronic universal testing machine, Shenzhen Sansi Longitudinal and Horizontal Technology Co., Ltd., China, UTM4024X.		
Constant temperature box, Shenzhen Sansi Longitudinal and Horizontal Technology Co., Ltd., China, WGDY-7300S.		
Electric sprayer, Wagner, Germany, FC3500.		
10000# screen mesh, Wuhan Xinshenshi Chemical Technology Co., Ltd., China.		
Anhydrous ethanol (EtOH), Wuhan Xinshenshi Chemical Technology Co., Ltd., China.		
Tetraethyl orthosilicate (TEOS), Wuhan Xinshenshi Chemical Technology Co., Ltd., China.		

RESOURCE AVAILABILITY

Lead contact

Further information and requests should be directed to and will be fulfilled by the lead contact, Heng Xie (hengxie@hust.edu.cn).

Materials availability

All materials were commercially available and did not need further purification, and this study did not generate new unique reagents. Polypropylene (PP; grade T30S) was purchased from Fujian Zhongjing Petrochemical Co., Ltd., China, and nano silica particles (SiO_2; grade R974) were procured from Evonik Industries AG, Germany. An electronic universal testing machine (UTM4024X, Shenzhen Sansi Longitudinal and Horizontal Technology Co., Ltd., China) coupled with a constant temperature box (WGDY-7300S, Shenzhen Sansi Longitudinal and Horizontal Technology Co., Ltd., China) were used for directional demolding. An electric sprayer (FC3500, Wagner, Germany) is used for spraying the SiO_2 nanoparticles on the sample surface. 10000# screen mesh, anhydrous ethanol (EtOH), and tetraethyl orthosilicate (TEOS) were supplied by Wuhan Xinshenshi Chemical Technology Co., Ltd.

Data and code availability

All data reported in this paper will be shared by the lead contact upon request.

This paper does not report original code.

Any additional information required to reanalyze the data reported in this paper is available from the lead contact upon request.

EXPERIMENTAL MODEL AND SUBJECT DETAILS

Preparation of tilt micro/nanopillars on the PP surface

The preparation process of the tilt micro/nanopillars on the PP surface is shown in below figure. Firstly, PP was dried in an air oven at 80°C for 2 h to remove moisture. 10000# screen mesh was then fixed to the inner surface of the mold, which was heated to 180°C. The PP melt is extruded by an eccentric rotor extruder and compressed under a pressure of 10MPa. After cooling and demolding, PP with screen mesh was obtained (below figure(Step 1)). Then, the screen mesh and the PP of the sample were fixed on the upper and lower fixtures of the electronic universal testing machine, respectively. After being held at temperature for 5 min in the constant temperature box (130°C), the samples were demolded at a stretch rate of 20mm min^{-1} to obtain 25-PP (demolding at 25°C) and 130-PP (demolding at 130°C) with tilt micropillars on their surface (below figure(Step 2)). Subsequently, 10 g of SiO_2 and 3 g of TEOS were added to 87 g of EtOH and ultrasonically treated for 30 min to prepare a SiO_2/TEOS solution. Then, 20 mL of SiO_2/TEOS solution was uniformly sprayed onto the tilt micropillars surface (100 × 20 mm^2) via an electric sprayer. Finally, the sprayed sample was dried in an oven at 80°C for 2 h to obtain a material with tilt micro/nanopillars (130-PP@SiO_2, below figure (Step 3)).

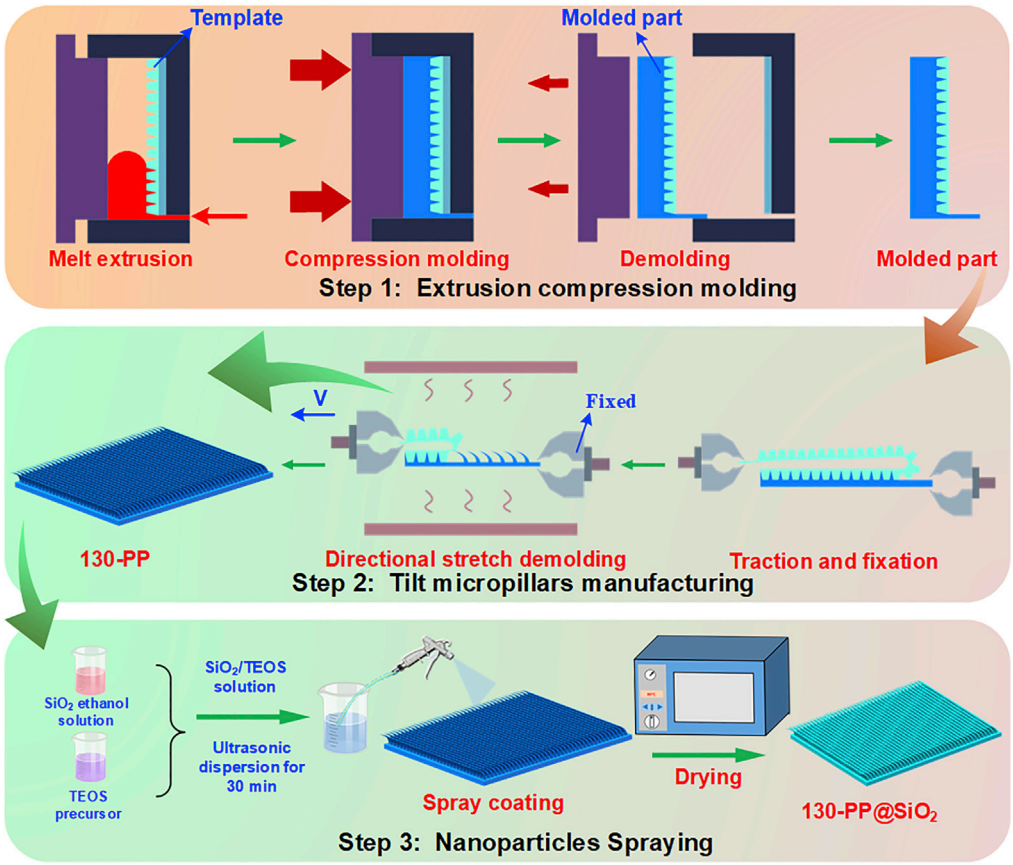

Preparation process of the surface with tilt micro/nanopillars

Characterization

Scanning electron microscopy (SEM; MIRA LMS, TESCN Bron, s.r.o., Czech Republic) was used to observe the morphology and cross-section of the sample at an acceleration voltage of 5 kV and vacuum degree of 1.2×10^{-3} Pa. The elemental composition of the tilt micro/nanopillars material was characterized using an energy dispersive X-ray spectrometer (Xplore, Oxford Instrument Technology Co., Ltd., UK) coupled with SEM; The contact angle (CA) and rolling angle (RA) of the sample surface were characterized using automatic CA testing apparatus (JC2000, Shanghai Zhongchen Co., Ltd., China). The CA and RA tests were conducted at five different locations to obtain average values, and the testing droplets were 5 μL. The rotation direction of $RA_{//}$ is consistent with the tilt direction of the micropillars, and the rotation direction of $RA_{\leftarrow}$ is opposite to the tilt direction of the micropillars. The rotation directions of RA_1 and RA_2 are perpendicular to the tilt direction of the micropillars. The dynamic wettability of the water droplets (diameter of ~3 mm, dropped from heights of 3 cm, 5 cm, 7.5 cm, 10 cm and 12.5 cm) impacting the tilt micro/nanopillars was recorded using a high-speed camera (UX100, Photron. Ltd, Japan). The tilt angle of the sample was controlled by a multi-angle motion platform (GFG40-40, Jiaduo Automation Equipment Co., Ltd., China). The *We* value of water droplets at a height of *h* can be calculated using Equation (9):

$$We = \frac{\rho v^2 l}{\gamma} \quad \text{(Equation 9)}$$

where ρ is the liquid density, v is the velocity, l is the characteristic length (water droplet diameter), and γ is the surface tension coefficient. The velocity (v) at height of h can be calculated as follows:

$$v = \sqrt{2gh} \quad \text{(Equation 10)}$$

where g is the gravity acceleration ($g = 9.8 m\ s^{-2}$). Combining Equations (9) and (10), the *We* values of water droplets falling from 3 cm, 5 cm, 7.5 cm, 10 cm, and 12.5 cm are 20.2, 33.7, 47.2, 67.4 and 80.9, respectively. To characterize the durability of the sample, sandpaper (2000#, 45 × 10 mm) was placed on the surface,

with a weight (100 g) placed on the sandpaper. The CA was measured every 10 cycles, for a total number of 50 cycles. Bonding-stripping tests were conducted on the sample surface using adhesive tape (Deli Group Co., Ltd., China). The CA was tested every 10 cycles of adhesive-stripping, over a total number of 50 cycles.

QUANTIFICATION AND STATISTICAL ANALYSIS

Our study does not include statistical analysis or quantification.